

# Physical, structural, and shielding properties of cadmium bismuth borate-based glasses

Cite as: J. Appl. Phys. **127**, 175102 (2020); <https://doi.org/10.1063/1.5143116>

Submitted: 20 December 2019 . Accepted: 11 April 2020 . Published Online: 01 May 2020

Y. S. Alajerami , D. A. Drabold , M. Mhareb, Kashi N. Subedi, Katherine Leslee A. Cimatu, and Gang Chen



[View Online](#)



[Export Citation](#)



[CrossMark](#)

Lock-in Amplifiers  
up to 600 MHz



# Physical, structural, and shielding properties of cadmium bismuth borate-based glasses

Cite as: J. Appl. Phys. 127, 175102 (2020); doi: 10.1063/1.5143116

Submitted: 20 December 2019 · Accepted: 11 April 2020 ·

Published Online: 1 May 2020



View Online



Export Citation



CrossMark

Y. S. Alajerami,<sup>1,2,a)</sup> D. A. Drabold,<sup>1</sup> M. Mhareb,<sup>3,4</sup> Kashi N. Subedi,<sup>1</sup> Katherine Leslee A. Cimatu,<sup>5</sup> and Gang Chen<sup>1</sup>

## AFFILIATIONS

<sup>1</sup> Department of Physics and Astronomy, Ohio University, Athens, 45701 Ohio, USA

<sup>2</sup> Medical Imaging Department, Applied Medical Sciences Faculty, Al Azhar University, 1277 Gaza, Palestine

<sup>3</sup> Department of Physics, College of Science, Imam Abdulrahman Bin Faisal University, P.O. Box 1982, 31441 Dammam, Saudi Arabia

<sup>4</sup> Basic and Applied Scientific Research Center, Imam Abdulrahman Bin Faisal University, P.O. Box 1982, 31441 Dammam, Saudi Arabia

<sup>5</sup> Department of Chemistry and Biochemistry, Ohio University, 100 University Terrace, 136 Clippinger Laboratories, Athens, 45701 Ohio, USA

<sup>a)</sup>Author to whom correspondence should be addressed: [Yasser.s.alajerami@gmail.com](mailto:Yasser.s.alajerami@gmail.com)

## ABSTRACT

We explore a new glassy material for radiation shielding applications. Novel transparent and non-toxic  $\text{Bi}_2\text{O}_3\text{-B}_2\text{O}_3$  glasses including different concentrations of CdO were prepared by the conventional melt quenching method. The prepared samples were characterized and analyzed by using various analytical tools (XRD, FTIR, Raman, DSC, and UV-Vis-NIR). *Ab initio* molecular dynamics simulations were carried out to create structural models of the materials, and these were compared to our measurements. To the best of our knowledge, this is the first study to compare the vibrations obtained experimentally with the vibrational density of states obtained from an *ab initio* computer model for these materials. The radiation shielding properties were measured for the photon energy range ( $10^{-3}\text{-}10^5$  MeV): both mass attenuation coefficient ( $\mu/\rho$ ) and effective atomic number ( $Z_{\text{eff}}$ ) showed a gradual increase with an increase in the CdO content. The mean-free-path, tenth value layer, half-value layer, and electron density for all prepared glasses were estimated. Promising results were achieved with the new glasses for radiation shielding purposes such as nuclear reactor and medical applications. The structural, electronic, and vibrational properties of the computer models revealed a topologically disordered, but chemically ordered network, and our vibrational computations provide direct insight into several Raman peaks observed for the materials.

Published under license by AIP Publishing. <https://doi.org/10.1063/1.5143116>

## I. INTRODUCTION

Medical imaging facilities employ ionizing radiation for diagnosis. This radiation has energy sufficient to penetrate and release electrons through its complex interaction with materials.<sup>1</sup> In human tissue, low risk is predicted if the released ions recombine; in this case, the probability of healing is high. There is particular concern regarding the long-time effects that may appear after years of absorbing low doses (such as leukemia, with a 10 year incubation period).<sup>2</sup> Thus, radiation shielding is required to protect operators, medical staff, and patients. There are three types of shielding: (1) structural shielding (barriers), (2) equipment-mounted shielding (source shielding), and (3) personal protective devices (goggles, gloves, and gonadal shielding).<sup>3</sup>

The efficacy of the shielding depends upon the intensity of the incident radiation and the physicochemical composition of the absorber material. For many years, concrete and heavy elements, such as lead (Pb), have been the standard choices, but these materials have many drawbacks in terms of stability, safety, and cost-effectiveness.<sup>4,5</sup>

Several studies have been conducted to improve shielding material properties by developing new alloys, ceramics, marbles, steel, polymers, and slag and lead-based glasses.<sup>6-13</sup> Due to their ease of fabrication, non-toxic nature, and cost effectiveness, lead-free glasses have been preferred in the literature to provide gamma-ray shielding.<sup>14-16</sup> Many glass formers such as borate,

tellurite, silicate, and germanium have been investigated for shielding purposes.<sup>16–19</sup>

The promising results obtained from borate glass materials during the last four decades motivate researchers to prepare and investigate related compositions and structures. These compositions find many industrial and medical applications. With their low density and highly hygroscopic character, borate glasses have advantageous features such as high mechanical strength, low melting point, high transparency, and low phonon energy.<sup>20–22</sup> Studies have demonstrated that small amounts of alkali and alkaline added as modifiers, and lanthanides (as dopants) improve borate properties.<sup>23–25</sup>

Modified borate glasses are a promising alternative due to their transparency, wide glass forming region, and cost effectiveness for recycling and construction.<sup>17–19</sup> Previous studies showed the efficiency of cadmium oxide (CdO) as a glass modifier.<sup>26–28</sup> At the same time, bismuth tri-oxide ( $\text{Bi}_2\text{O}_3$ ) appears to be a promising modifier in borate-based glass and has broad applications for laser host fibers and for photonic switches. Due to the high molecular weight (465.96 g mol<sup>-1</sup>), density (8.9 g cm<sup>3</sup>), and optical transparency of bismuth trioxide, bismuth-borate glasses attract researchers to investigate their shielding properties.<sup>29–31</sup> Therefore, a boron-glass network modified with small amounts of cadmium oxide and bismuth tri-oxide can acquire high density and, as we show, it turns out to be a good ionizing radiation absorber.

In the current study, structural, physical, and radiation shielding properties such as mass attenuation coefficients ( $\mu/\rho$ ), Half-Value Layer (HVL), Tenth-Value Layer (TVL), Mean Free Path (MFP), and the effective atomic number ( $Z_{\text{eff}}$ ) of bismuth borate glasses modified with different amounts of cadmium oxides were investigated as a function of  $\text{B}_2\text{O}_3$  content. In addition, this study shows a comparison between *ab initio* molecular dynamics (AIMD) simulation and experimental results in exploring some structural and optical properties.

## II. METHODS

### A. Sample preparation

The current samples were prepared in the Department of Physics and Astronomy at Ohio University. Based on the melt quenching method, a series of bismuth-borate glasses were prepared by using the following raw materials: boron oxide ( $\text{B}_2\text{O}_3$ ), bismuth oxide ( $\text{Bi}_2\text{O}_3$ ), and cadmium oxide (CdO). Care is required to avoid inhalation when adding CdO, as fumes and dust are intensely irritating to respiratory tissue. All chemicals were obtained from Alfa Aesar with high purity (99.5% and above). The compositions were well mixed by using a mechanical mixer for more than 60 minutes. An electrical furnace was used to melt the material at 1100 °C for 60 to 70 min. For each prepared sample, the crucible was shaken once after the first 60 min. The molten glass was poured into stainless steel located inside another furnace at 300 °C (below its glass transition temperature) for 3 h to relieve thermal stress, for structural stabilizing, and to reduce the number of voids and defects. Finally, the prepared glasses were polished and cut to 3 mm thickness. Nomenclature, compositions, and labels for the purpose of this paper are reported in Table I. The prepared glass was highly transparent, and it gradually changed into brown with the increase of  $\text{Bi}_2\text{O}_3$ , as shown in Fig. 1.

**TABLE I.** Chemical composition of the prepared glasses.

Glass label	Composition (mol%)		
	CdO	$\text{Bi}_2\text{O}_3$	$\text{B}_2\text{O}_3$
G1	0	30	70
G2	5	30	65
G3	10	30	60
G4	15	30	55

### B. Computational details

*Ab initio* molecular dynamics (AIMD) simulation using projected-augmented wave (PAW) potentials<sup>32,33</sup> was employed as implemented in the Vienna *ab initio* simulation package (VASP)<sup>34</sup> to make the current models. The generalized gradient approximation (GGA) of Perdew–Burke–Ernzerhof (PBE)<sup>35</sup> was used to approximate the Density Functional Theory (DFT) exchange correlation functional. Plane waves up to 400 eV were used as the basis set. A single k-point ( $\Gamma$ ) to sample the Brillouin zone was used with the periodic boundary conditions throughout.

Four different models of the general form  $(\text{B}_2\text{O}_3)_{0.7-x}(\text{Bi}_2\text{O}_3)_{0.3}(\text{CdO})_x$  with  $x = 0, 0.05, 0.10$ , and  $0.15$  were generated to represent the new prepared glasses G1, G2, G3, and G4, respectively. For each model, a supercell of 100 atoms was created at the experimental density reported in Sec. II C. Atoms were placed randomly in the supercell with a minimum separation of 2 Å. The models were created based on the quench-from-melt method.<sup>36</sup> For each model, the initial random configuration was heated from room temperature to 3000 K at a rate of 0.2 K/fs and then equilibrated at 3000 K for 4.5 ps. The model at 3000 K was cooled in successive steps to 1000 K and 300 K at the same cooling rate of 0.2 K/fs followed by equilibration for 4.5 ps and 6 ps, respectively. For all molecular dynamics simulation, a time step of 1.5 fs was used and the temperature was controlled by a Nosé–Hoover thermostat.<sup>37</sup> The model at 300 K was then fully relaxed by using the conjugate gradient method implemented in VASP.

The lattice dynamics of the glasses was studied by computing the vibrational density of states (VDOS), the species projected VDOS, and the localization of the vibration eigenstates. For each relaxed model, the dynamical matrix elements were computed in the harmonic approximation by perturbing each atom along the



**FIG. 1.** The newly prepared glasses (G1–G4).

$\pm x$ ,  $\pm y$ , and  $\pm z$  directions by 0.015 Å. The diagonalization of the dynamical matrix yields the phonon eigenvalues and the corresponding eigenvectors. The normalized VDOS and the partial VDOS are expressed as<sup>38</sup>

$$Z(E) = \sum_i \delta(E - \hbar\omega_n), \quad (1)$$

$$Z_\alpha(E) = \frac{1}{3N} \sum_{i \in \alpha}^{N_\alpha} \sum_n |e_i^n|^2 \delta(E - \hbar\omega_n), \quad (2)$$

where  $\omega_n$  are the normalized eigenvalues and the sum over  $i$  is over all the atoms belonging to the particular species  $\alpha$ .  $e_i^n$  represents the displacement vector of atom  $i$  with components  $e_{ui}^n$ , where  $= x$ ,  $y$ , and  $z$ . The delta functions in Eqs. (1) and (2) were approximated by a gaussian of width 15 cm<sup>-1</sup>. The localization of the vibrational eigenstates was studied by computing the inverse participation ratio (IPR) from the normalized displacement vectors. The IPR is defined as

$$IPR = \frac{\sum_{i=1}^N |e_i^n|^4}{(\sum_{i=1}^N |e_i^n|^2)^2}. \quad (3)$$

The magnitude of IPR ranges from 0 to 1. Localization modes have a higher IPR.

### C. Density measurements and related parameters

The densities ( $\rho$ ) of the current glasses in addition to a series of significantly related parameters were determined based on the equations and mathematical expressions listed in supplementary material (A).

The glass durability of the new compositions was calculated from the dissolution rate (DR) expression listed in Appendix A.<sup>39</sup> The DR value was measured at two different temperatures (25 °C and 80 °C). The glasses were prepared in cube shapes with dimensions of (5 × 5 × 2) mm<sup>3</sup>. The samples were shaken in a jar filled with distilled water (100 cm<sup>3</sup>) for a period of two weeks.

### D. Characterization techniques employed

An array of experimental probes was deployed to determine microstructure and other properties of the glasses. Among these were x-ray Diffraction (XRD), differential scanning calorimetry (DSC), Fourier transform infrared (FTIR), and Raman and Ultraviolet-VISIBLE-Near Infrared Spectroscopy (UV-Vis-NIR).

An x-ray diffractometer (XRD) model Rigaku MiniFlex II was used to study the amorphous nature of the prepared samples. The scanning range was  $2\theta = 10^\circ - 80^\circ$  with a consecutive step of  $0.01^\circ - 20$ . The x-ray was produced by using a generator power of 40 kV and 30 mA, and the spectra were recorded using CuK $\alpha$  as a target ( $\lambda = 1.5406$  Å) with a scanning rate of  $2^\circ$  per minute. To get an insightful study about the structural groups of the prepared glass, FTIR spectra were recorded by using a Nicolet 380 FTIR Spectrometer. The samples were ground and mixed with KBr

(1:100) to create small pellets with 1–1.5 mm thickness. All spectra were recorded at room temperature in the wavenumber range of 400–2500 cm<sup>-1</sup>. The Raman characterization was explored by using R-3000 (PhotoniTech PvT). The room temperature absorption and reflection spectra of the glasses were recorded by using a UV-Vis-NIR Agilent 8453 absorption spectrophotometer in the wavelength region of 200 nm to 900 nm. The glass-forming ability (GFA) of the prepared glasses was checked by using the common glass stability (GS) parameters. These parameters rely on thermal properties obtained from differential scanning calorimetry (SETARAM SETYS 16 TG-DSC), which are as follows: the onset glass transition temperature ( $T_g$ ), onset crystallization temperature ( $T_{on}$ ), peak crystallization ( $T_c$ ), crystallization temperature ( $T_c$ ), and melting temperature ( $T_m$ ).

### E. Radiation shielding and attenuation properties

The radiation shielding properties of the prepared samples, such as the mean free path (MFP), tenth value layer (TVL), effective atomic number ( $Z_{eff}$ ), and effective electron number ( $Ne$ ) were calculated based on the mass attenuation coefficient ( $\mu$ ) obtained from the online computer program [supplementary material (B)]. This well-known computer program (developed by Breger and Hubbell)<sup>40</sup> is known as XCOM and was developed at the National Institute of Standards and Technology (NIST/USA). This software offers the possibility for calculating the cross section and attenuation coefficient for elements, compounds, and mixtures at different photon energies (from 1 keV to 100 GeV) and different photon-material interactions. The possibility of interaction was estimated based on the cross sections for photoelectric absorption, Compton and coherent scattering, and pair production.

## III. RESULTS

### A. Computer models

#### 1. Topology

In order to describe the atomic structure of the prepared glasses, four models of Bi<sub>2</sub>O<sub>3</sub>–B<sub>2</sub>O<sub>3</sub> with different concentrations of CdO are presented in Fig. 2. The models are dubbed M<sub>1</sub>, M<sub>2</sub>, M<sub>3</sub>, and M<sub>4</sub> for the prepared glasses. The majority of B atoms form the BO<sub>3</sub> structure with very few tetrahedral structures (BO<sub>4</sub>). The distorted boroxol rings (B<sub>3</sub>O<sub>6</sub>) are present in our glass models M<sub>1</sub>, M<sub>3</sub>, and M<sub>4</sub>. The modifiers in the glass are mostly bonded with the non-bridging O atoms of the BO<sub>3</sub>. The Bi atoms are more or less uniformly scattered in the glass without any physical bond less than 3 Å. The Cd atoms are mostly bonded with the O atoms. The coordination of Cd with O decreases with the increase in the CdO concentration because the number of O atoms is more or less the same in all models.

The structure of the glass models was characterized by the pair correlation functions  $g(r)$ , shown in Fig 3.

Two well-defined peaks are observed in  $g(r)$  for all models. The partial pair correlation functions were also calculated to determine the origin of the peaks. We find that the first peak is due to the B-O bonding, and the intensity of the peak decreases with increasing CdO content. Thus, the coordination of the B with O decreases with increasing CdO content. The second peak around

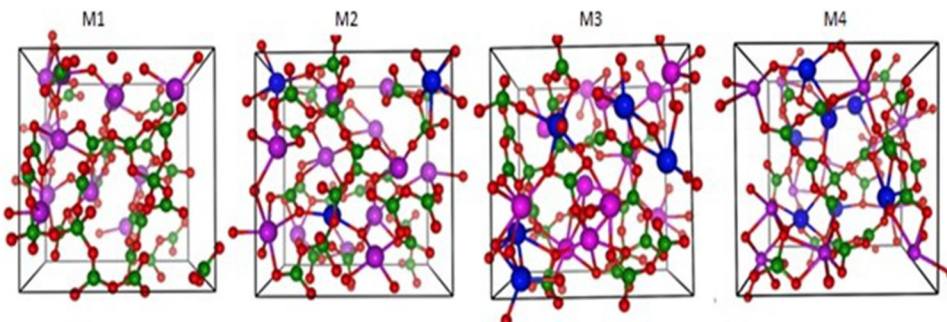


**FIG. 2.** Optimized atomistic structures for  $(\text{B}_2\text{O}_3)_{0.7-x}(\text{Bi}_2\text{O}_3)_{0.3}(\text{CdO})_x$  models. Atom colors: Green (B), red (O), magenta (Bi), and blue (Cd).

$\approx 2.39 \text{ \AA}$  is possibly due to the superposition from different bond pairs other than B–O pairs. The peaks for the B–B, Bi–O, Cd–O, and O–O pairs lie at 2.50, 2.32, 2.26, and 2.40  $\text{\AA}$ , respectively.

## 2. Electronic structure

The electronic structure of each model was studied by analyzing the electronic density of states (EDOS). Here, we simply examine the distribution of Kohn–Sham eigenvalues. Models M<sub>1</sub>, M<sub>3</sub>, and M<sub>4</sub> had a defect-free bandgap, whereas model M<sub>2</sub> had a defect state pinned close to the Fermi level. The bandgap for the glass samples was estimated experimentally by Tauc's plot obtained from the UV-Vis-NIR absorption spectra [supplementary material (C)]. The bandgap from the glass models and the experiment are shown in Fig. 4(a). In both theoretical models and experimental calculations, the bandgap monotonically decreases with the increase of CdO with pleasingly similar slopes. As expected, DFT underestimated the gap (by  $\approx 0.49 \text{ eV}$ ) compared with the experimental data. Figure 4(b) shows the EDOS obtained from model M<sub>2</sub>, where the small peak near the Fermi level represents the defect state. To understand this defect electronic state, the partial charge

density was calculated by integrating the electronic densities for the energy range where the defect lies. The inset in Fig. 4(b) shows the structure and the partial charge density. The defect states (yellow blobs) are due to the under-coordinated Bi atoms.

## B. Properties of the samples

### 1. Density measurements and related parameters

Several physical parameters such as molar fraction, ion concentrations ( $N$ ), inter-ionic distance ( $r_i$ ), polaron radius ( $r_p$ ), and other significant physical parameters are calculated and listed in Table II.

The density of the prepared glass system increased with increasing the cadmium oxide content from  $4.315 \pm 0.005$  to  $5.375 \pm 0.016 \text{ g cm}^{-3}$  for samples G1 to G4 (Table II). This increase is expected and attributed to the higher molecular weight of CdO compared with that of  $\text{B}_2\text{O}_3$ . Moreover, CdO is heavier (128.4 amu) than  $\text{B}_2\text{O}_3$  (69.62 amu).

A decrease in the molar volume was reported with an increase in the CdO content (Table II). The reduction in molar volume with an increase in density gives a good indication of the compactness of the prepared glasses. It may be assumed that the increase in the CdO concentration at the expense of  $\text{B}_2\text{O}_3$  caused the opened glass network structure.<sup>41</sup> Generally, there is an indirect relation between density and molar volume, and many studies reported the same behavior.<sup>19,21,24</sup>

The density depends on the multi-composition of the glass network. Eventually, higher structure compactness will produce higher density of the glass. The increment in density indicates that the number of oxygen packing density (OPD) in the glass network increases and decreases in non-bridging oxygen. On the contrary, the value of the oxygen molar volume decreases with an enhancement of CdO. The oxygen molar volume decreases opposite to the oxygen packing density with the increasing CdO content in glasses, indicating tight packing of the glass network by increasing the bridging oxygen bond. The same trend was reported with molar refractivity ( $R_M$ ), which increased gradually with the increasing CdO (21.479–27.033). The Poisson ratios of the current glasses were  $>0.3$  and increased with the CdO concentration. The direct relation between cadmium oxide concentration, refractive index, dielectric constant, and polarizability was attributed to an increase in ionic concentration, which proved the compactness of the prepared glasses.<sup>42–44</sup> The same relation was reported with the optical

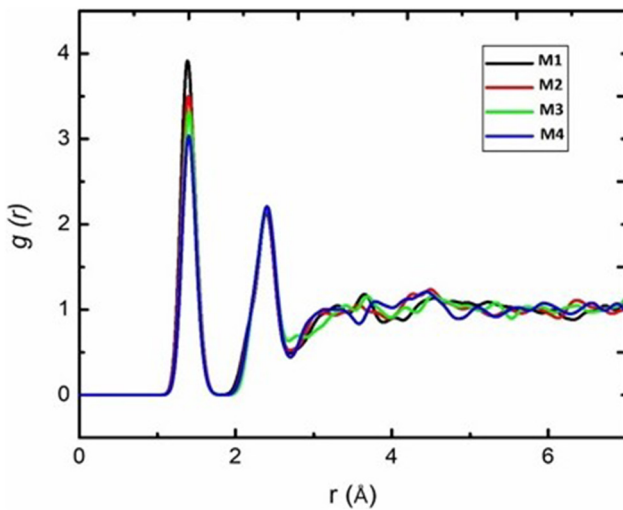


**FIG. 3.** Pair correlation function  $g(r)$  obtained from models M<sub>1</sub>, M<sub>2</sub>, M<sub>3</sub>, and M<sub>4</sub>.

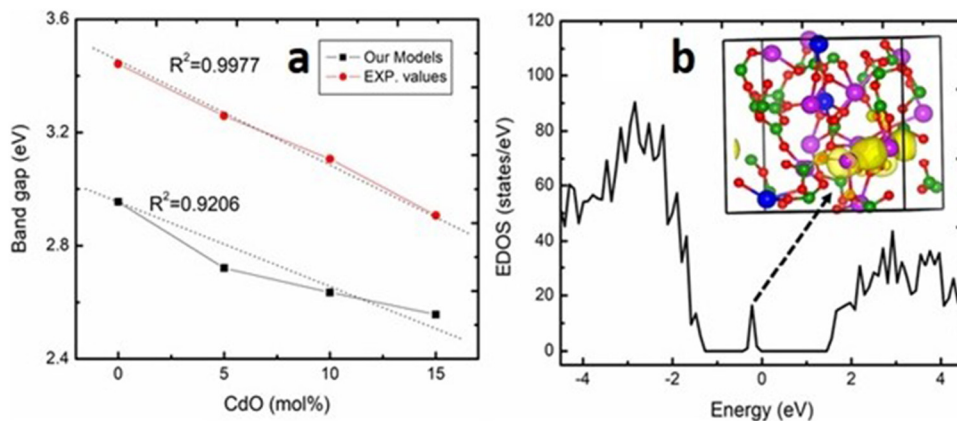


**FIG. 4.** (a) (Left) The electronic bandgap calculated from the optimized models and from the experiment. (b) (Right) The EDOS calculated from model M<sub>2</sub>. The inset shows the partial charge density (yellow blobs) on model M<sub>2</sub>. The atom color is the same as Fig. 2. The charge density is mostly localized in the under-coordinated Bi atoms.

basicity. An enhancement in the reflection loss (R) values was reported in all glass samples with increasing the CdO content. This trend indicates that the reflection back of energy reduced by increasing the chromium content.

## 2. Glass durability

Concerning the durability of the prepared glass, we report that the dissolution rates (DR) increased with time (up to 2 weeks) and decreased with an increase in the CdO content (Table III). The increase in DR with increasing immersion time was attributed to

**TABLE II.** Density and related parameters of Bi-Bo glass with different concentrations of CdO. Each symbol is defined in the [supplementary material](#) (A).

Parameter	Unit	G1	G2	G3	G4
P	g cm <sup>-3</sup>	4.315	4.711	5.068	5.375
V <sub>m</sub>	cm <sup>3</sup> mol <sup>-1</sup>	46.689	40.641	38.358	36.714
V <sub>o</sub>	cm <sup>3</sup> mol <sup>-1</sup>	14.563	14.014	13.699	13.598
V <sub>t</sub>	...	0.512	0.537	0.553	0.562
OPD	g atom l <sup>-1</sup>	68.667	71.357	72.996	73.541
$\sigma$	...	0.229	0.241	0.249	0.253
$\langle d_{B-B} \rangle \times 10^3$	Nm	0.403	0.321	0.265	0.226
$N \times 10^{22}$	Ions cm <sup>-3</sup>	...	0.741	1.570	2.461
$r_p \times 10^{-15}$	Å	...	1.177	0.555	0.354
$r_i \times 10^{-15}$	Å	...	4.498	2.123	1.354
E <sub>g</sub> (direct)	eV	3.442	3.259	3.106	2.907
E <sub>g</sub> (indirect)	eV	3.841	3.580	3.381	3.259
Urbach energy	eV	0.213	0.236	0.269	0.293
$\Delta E$					
N		2.287	2.331	2.3691	2.426
X		0.925	0.876	0.835	0.781
R		0.585	0.596	0.606	0.619
R <sub>M</sub>		21.479	22.879	24.625	27.033
$\alpha_M \times 10^{-24}$	(cm) <sup>3</sup>	8.519	9.073	9.770	10.107
E		5.229	5.432	5.613	5.869
P		4.229	4.432	4.613	4.869
$\Lambda$		0.991	1.013	1.015	1.027

the possibility of ion exchange and glass network hydration.<sup>45</sup> Conversely, the dissolution decreased with increasing CdO content. Based on the calculated physical properties (Table II), the increment of cadmium oxide led to increasing glass density and BO<sub>4</sub> units as well. This result proved the ability of CdO to improve the water resistance of bismuth borate glass.

## 3. Structural and thermal properties of the glasses

The XRD patterns of the new glasses (G1-G4) are shown in Fig. 5. The XRD plots for each sample show an evident broad peak with a maximum height at 27° (2θ). The absence of sharp peaks in all patterns is indicative of the amorphous nature of these samples.

Next, we studied DSC for G1 in Fig. 6 with labels pertaining to each thermal transition from 100 °C to 1100 °C. The inset figure presents the DSC plots for G2, G3, and G4. The glass transition temperature (T<sub>g</sub>) in the G<sub>1</sub> sample (without cadmium) is reported to be 370 °C, whereas bismuth borate glass with 5 mol% CdO has a T<sub>g</sub> of 360 °C. Therefore, by adding CdO into binary bismuth borate glass to form ternary 30Bi<sub>2</sub>O<sub>3</sub> + 70 - xB<sub>2</sub>O<sub>3</sub> - xCdO glass (x = 5, 10, and 15 mol%), the glass transition temperature first decreases, and then with a further increase in the CdO concentrations to 10 mol% and 15 mol%, its value increases gradually (Table IV).

The DSC values (T<sub>g</sub>, T<sub>onp</sub>, T<sub>C</sub>, and T<sub>m</sub>) have been estimated from the exact middle point on the endothermic or exothermic regions in the thermos graph. The T<sub>C</sub> peaks broadened and decreased in intensity with the increment of the CdO content, which indicates that glass stability against devitrification enhances by adding CdO. The

**TABLE III.** Dissolution rates of glass samples as a function of time and composition.

Sample label	DR (2 days) g cm <sup>-2</sup> d <sup>-1</sup>	DR (7 days) g cm <sup>-2</sup> d <sup>-1</sup>	DR (14 days) g cm <sup>-2</sup> d <sup>-1</sup>
G1	$7.523 \times 10^{-7}$	$5.701 \times 10^{-6}$	$1.291 \times 10^{-5}$
G2	$7.202 \times 10^{-7}$	$4.317 \times 10^{-6}$	$8.837 \times 10^{-6}$
G3	$3.022 \times 10^{-7}$	$1.363 \times 10^{-6}$	$2.415 \times 10^{-6}$
G4	$1.415 \times 10^{-7}$	$5.328 \times 10^{-7}$	$7.449 \times 10^{-7}$

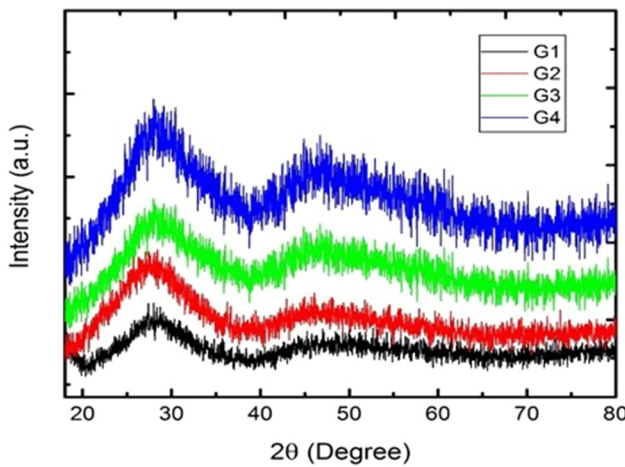


FIG. 5. XRD spectra of the prepared samples. The plots for the different glass samples are displaced in the y axis for the purpose of clarity.

higher values obtained from the temperature difference ( $\Delta T = T_c - T_g$ ) for all samples reflect the higher thermal stability of the prepared glasses.<sup>46</sup> Also, the low values of the reduced glass transition temperature ( $T_{rg} = T_g/T_m$ ) confirm the good tendency for glass formation against crystallization for the prepared glasses.<sup>47</sup>

### C. Joint experimental/modeling analysis of vibrations

The vibrational modes in the glasses were probed by FTIR spectra (Fig. 7) and Raman spectra (Fig. 8). The interpretation of vibrations was enabled using the vibrational density of states obtained from the optimized computer models (Figs. 9 and 10).

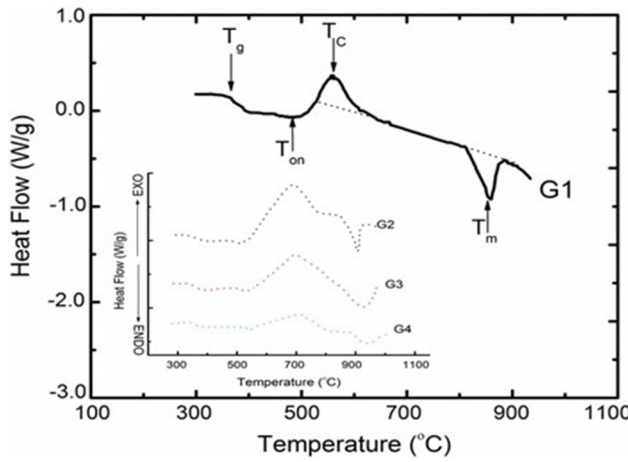


FIG. 6. DSC thermographs of  $x\text{-CdO-Bi-Bo}$  glasses at a heating rate of  $10^{\circ}\text{C} \cdot \text{min}^{-1}$ . ( $T_g$ : glass transition;  $T_{on}$ : onset crystallization temperature;  $T_c$ : crystallization temperature;  $T_m$ : melting temperature).

TABLE IV. Thermal analysis using differential scanning calorimetry for the prepared glasses.

Sample label	$T_g$ ( $^{\circ}\text{C}$ )	$T_{on}$ ( $^{\circ}\text{C}$ )	$T_c$ ( $^{\circ}\text{C}$ )	$T_m$ ( $^{\circ}\text{C}$ )	$\Delta T$ ( $^{\circ}\text{C}$ )	$T_{rg}$ ( $^{\circ}\text{C}$ )
G1	370	491	582	850	212	0.435
G2	360	485	690	905	330	0.396
G3	365	508	693	910	328	0.401
G4	372	525	696	912	324	0.408

The FTIR spectra in Fig. 7 have been normalized by using the MIN MAX method.<sup>48</sup> There are distinct vibrations at  $600\text{--}650\text{ cm}^{-1}$ , and these vibrations shift to a higher wave number with an increase in the CdO concentration. In addition, an obvious band was detected at  $650\text{--}700\text{ cm}^{-1}$  in all glass samples. Previous studies attributed this vibration to the bismuth ions,<sup>48,49</sup> but usually this band is attributed to the known bending and stretching vibrations of NBO with  $\text{BO}_3$  units. At  $820\text{--}900\text{ cm}^{-1}$ , we reported an increase in the stretching vibration intensity with the addition of CdO. This band was also shown in Refs. 26 and 50, which attributed this vibration to the creation of non-bridging oxygen of  $\text{BO}_4$  units. At higher energies ( $1000\text{--}1400\text{ cm}^{-1}$ ), the shifting of peaks and shoulders toward a high wavenumber was clear. Previous studies assumed that this shifting was attributed to the asymmetric stretching vibrations of the created  $\text{BO}_4$ .<sup>51-55</sup> Furthermore, the addition of CdO showed a prominent peak and band at  $1200\text{ cm}^{-1}$  and  $1450\text{ cm}^{-1}$ , respectively. These peaks and bands shifted to a high wavenumber and enhanced with an increase in the CdO concentration. This result is consistent with previous related studies<sup>26,56</sup> which attributed this vibration to the stretching of B-O (linkage between oxygen and different groups) and also between boroxol rings and trigonal units of  $\text{BO}_3$ .

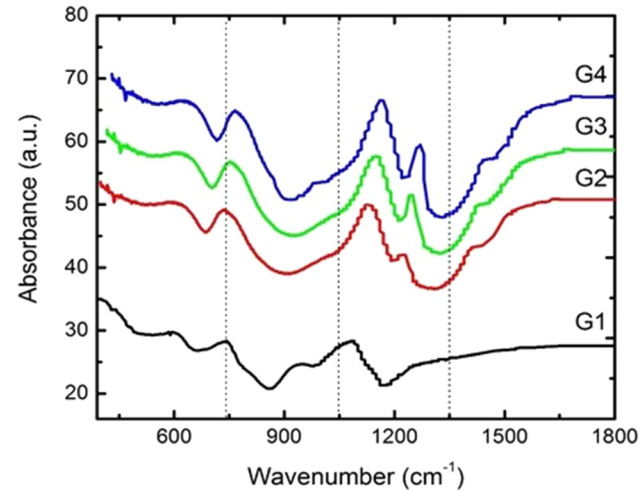
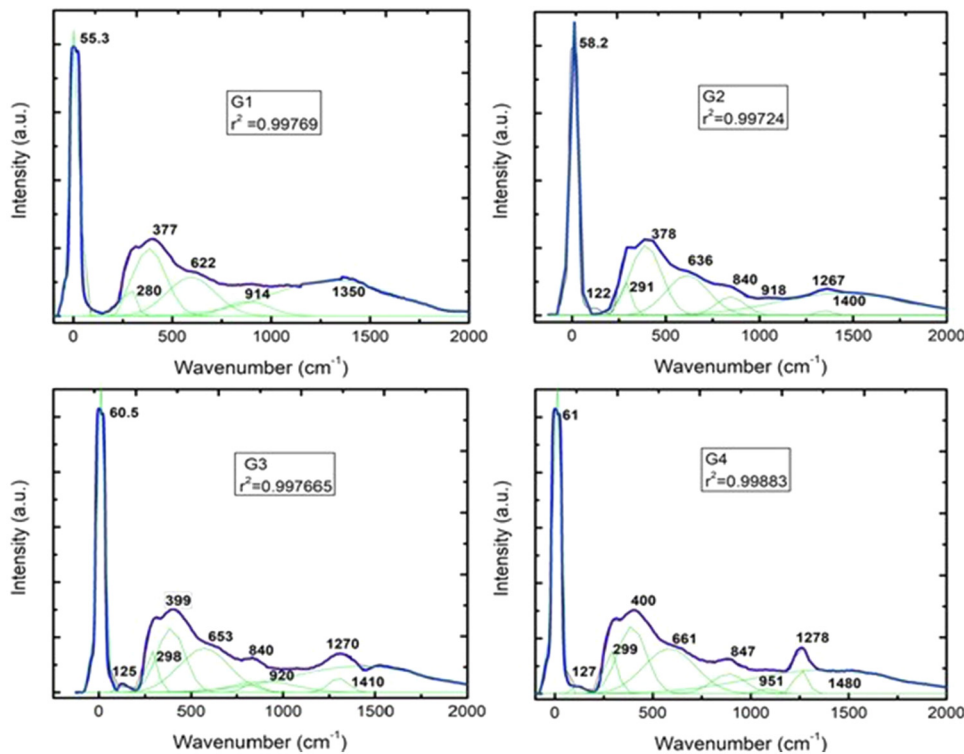


FIG. 7. FTIR spectra of bismuth borate glasses at different concentrations of CdO. The IR plots are displaced for clarity.



**FIG. 8.** De-convoluted Raman spectra of the prepared glasses.

Figure 8 shows the Raman bands of the new glasses. A de-convoluted Raman spectrum of six to nine peaks fitting was created to facilitate interpretation by using the “peak analyzer” module of Origin Pro 9 software. Generally, broad bands and peaks are observed in the range of analysis ( $0\text{--}2000\text{ cm}^{-1}$ ), with one intense peak located at the low wavenumber region. Previous studies<sup>49,50</sup> attributed the peaks located at 55, 280, 377, and  $412\text{ cm}^{-1}$  to the translational motion of  $\text{B}_2\text{O}_3$  with Bi. Another broad peak is observed at  $630\text{ cm}^{-1}$  and this peak is attributed by previous studies<sup>50,51</sup> to the vibration of the boron–oxygen bond in  $\text{BO}_3$  and the stretching of B–O–B in the metaborate ring as well. In addition, a small peak and broadband are reported at 914 and  $1400\text{ cm}^{-1}$ , respectively.

Previous related studies attributed the above to the vibrations of B and O in trigonal  $\text{BO}_3$  and tetrahedral  $\text{BO}_4$ .<sup>48–50</sup> Also, small peaks are observed at  $120\text{ cm}^{-1}$  and  $1270\text{ cm}^{-1}$  in the Cd-glasses (G2, G3, and G4), and the same peaks are reported by Chryssikos and Kamitsos.<sup>56</sup> The peak near  $120\text{ cm}^{-1}$  is attributed to the direct vibration of CdO, and the peak near  $1270\text{ cm}^{-1}$  is ascribed to the enhancement of B and O vibrations by the existing Cd atoms.<sup>57</sup> Both Bi and Cd are expected to vibrate at low frequency, and there is an increase in the CdO effect on the high frequency vibrations of the lighter elements (B and O) by the formation of di-borate, ortho-borate, and pyro-borate groups. Consequently, the compactness of the glasses increases systematically with the increase in CdO. In this study, we try to correctly determine the molecular vibrations by comparing them with the vibrational modes obtained from the dynamical matrices associated with each computer model.

Figure 9 exhibits the vibrational density of states (VDOS) obtained from the optimized computer models. The three observed peaks are circled as R<sub>1</sub>, R<sub>2</sub>, and R<sub>3</sub>. The intensity of the first peak in R<sub>1</sub> ( $\sim 63\text{ cm}^{-1}$ ) increases with an increase in CdO and slightly shifts

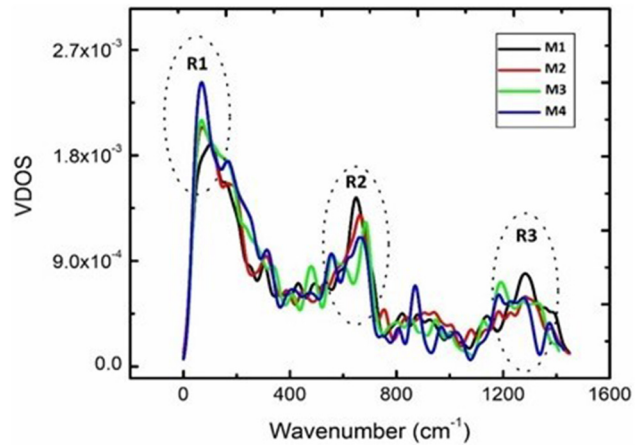


**FIG. 9.** Total VDOS obtained from the glass models. The smearing width of  $15\text{ cm}^{-1}$  was used for all models to approximate the delta function. The circled regions (R<sub>1</sub>, R<sub>2</sub>, and R<sub>3</sub>) are a guide for the eye to show the peaks at different frequency regimes.

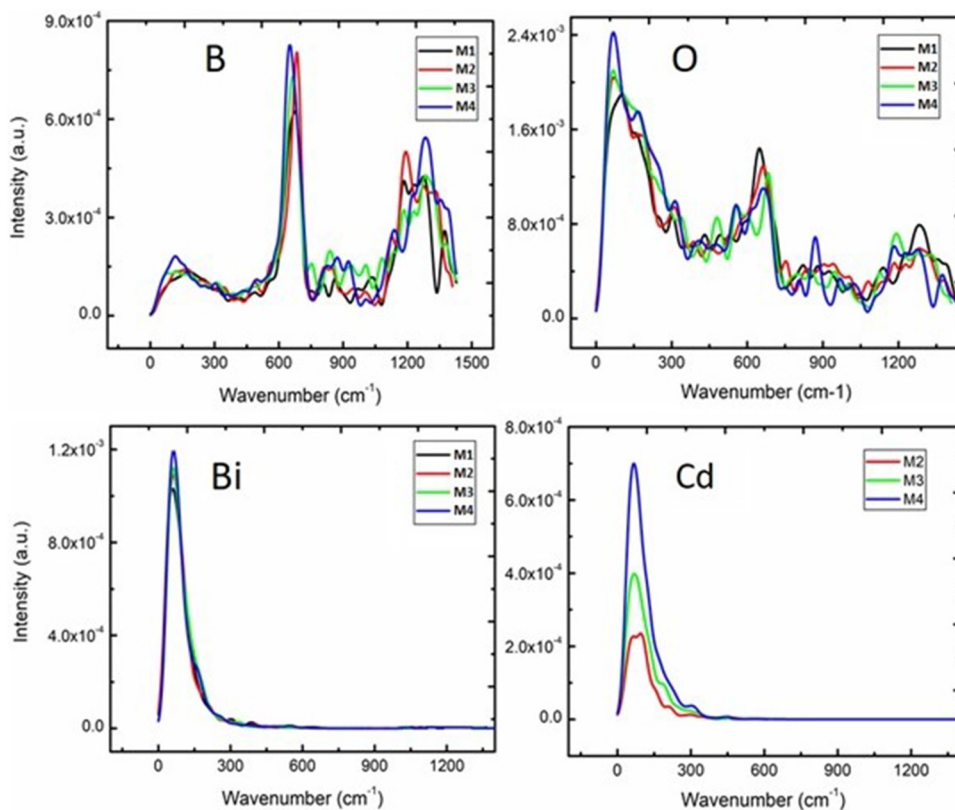


**FIG. 10.** Partial VDOS for varying CdO concentrations.

toward a lower frequency. Another peak is observed in R<sub>2</sub> ( $\sim 650$ – $700$  cm $^{-1}$ ) which shifts toward a higher frequency compared with M<sub>1</sub> (the sample without CdO content). At high frequency (R<sub>3</sub>), the two peaks are at frequencies  $\sim 1175$  and  $\sim 1275$  cm $^{-1}$ . To better understand the vibrations in these regions, the VDOS was projected onto atomic species as defined in Eq. (2).

Figure 10 shows the partial VDOS obtained from the glass models. To identify the nature of the vibration modes, we chose representative modes that were close to the peaks in the Raman spectra. In addition, animations showing these modes can be found in [supplementary material \(D\)](#). The spectra in Fig. 10 illustrate that the vibrations of heavy atoms (Bi and Cd) dominate the vibrations in the low frequency region (i.e., 60 cm $^{-1}$  and 120 cm $^{-1}$ ). These peaks are very consistent with the peaks observed in the Raman spectra (Fig. 8). The peak observed near 63 cm $^{-1}$  is mostly due to the bending motion of the Bi and Cd atoms. The bending vibration was dominant between Bi–O and Cd–O, with few stretching modes between Bi and O [Animations 1–3 in [supplementary material \(D\)](#)]. Thus, the growing peaks at  $\sim 120$  cm $^{-1}$  shown in Raman spectra are attributed to CdO vibrations, and this result is in agreement with the results of Chryssikos and Kamitsos.<sup>56</sup> The well-defined peak that occurs near 660 cm $^{-1}$  mainly emanates from the vibration of the boron and oxygen atoms, as shown in Fig. 10. These frequencies are also observed in the Raman spectra shown in Fig. 8. Animations 4 and 5 ([supplementary material](#)) show a strong

mixing of vibration modes close to this frequency. Both the bending and the stretching modes of the BO<sub>3</sub> rings are present, with the former dominating in the network (wagging motion), and the vibration from BO<sub>4</sub> is also recognized. There is no obvious vibration of Bi atoms at this energy level as mentioned in previous studies.<sup>48, 49</sup> In parallel, a weak bending vibration between Cd–B was reported at this level (Animation 5 in the [supplementary material](#)). Regarding the peak near the far end of the spectrum at around 1278 cm $^{-1}$ , it is mostly due to the stretching bonds of the BO<sub>3</sub> rings [Animations 6 and 7 in [supplementary material \(D\)](#)]. As we have reported before, it is often an oversimplification to describe vibrations in glasses as simple molecular modes—especially in intermediate frequency ranges, they instead tend to be mixed modes of different types.

The disorder in the glass network causes some of the vibrational modes to be localized. To understand the localization of the vibrational modes, the vibrational IPR from model M<sub>4</sub> (the highest CdO content) was calculated using Eq. (3), as shown in Fig. 11 (top plot). The IPR was further projected into atomic species, as shown in Fig. 11 (four bottom). It can be seen that the low frequency modes corresponding to the heavy atoms (Bi and Cd) are extended. The intermediate modes and the higher frequency modes are mostly localized in the B atoms. The higher frequency modes corresponding to the O atoms are extended.

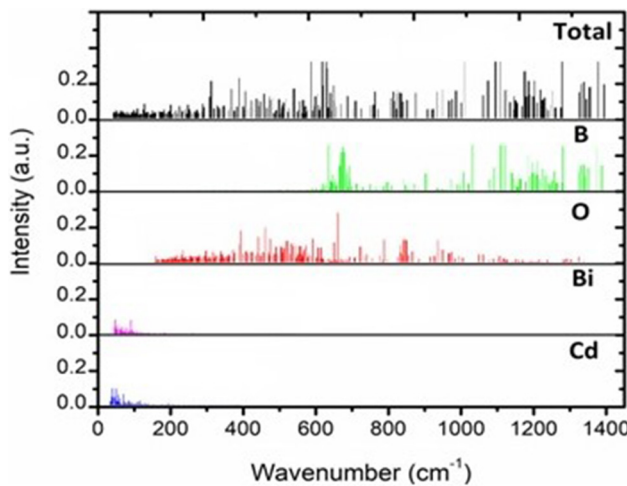


**FIG. 11.** Localization of vibrational modes. Top: IPR calculated using Eq. (3). Bottom: Spectral weight of IPR projected onto the atomic species represented by labels in each plot.

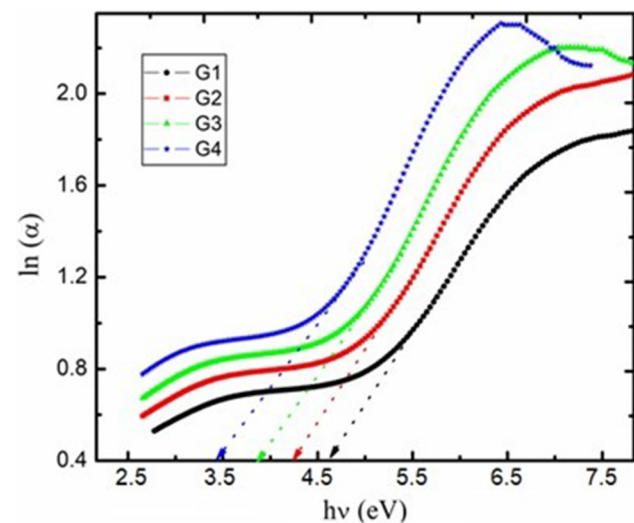


**FIG. 12.** Urbach Energy for  $\text{XCdO}-30\text{Bi}_2\text{O}_3-(70-x)\text{B}_2\text{O}_3$ .

## D. Optical absorption measurements

### 1. Metallization

The metallization of the current samples was estimated based on the formula listed in [supplementary material](#) (A). The increment of CdO reduces the metallization values, which agreed with the narrowing of the bandgap.<sup>57</sup> The estimated values of all prepared samples were  $>1$  and this confirms the non-metallization nature of the prepared samples.

### 2. Urbach energy

The Urbach energy of the current glasses was calculated by measuring the reciprocal of the straight-line slope of the curve in [Fig. 12](#). This curve represents the relation between the natural logarithm of the absorption coefficient ( $\ln \alpha$ ) and the incident photon energy ( $h\nu$ ). The calculated values of  $\Delta E$  are listed in [Table II](#), which clearly show a direct relation between  $\Delta E$  and CdO concentration. The minimum value of  $\Delta E$  was reported with G<sub>1</sub> (0 mol%

of CdO), and by an increment of CdO, the  $\Delta E$  increased up to 0.38 eV (the highest concentration of CdO). This behavior hints that the degree of disorder and defect inside the glass network increased with an increase in the CdO content. This defect led to the formation of localized states close to the conductive band level, which led to an increase in the band tail width.<sup>58</sup> The bandgap values of the prepared glasses decreased with an increase in the CdO content, and this may be attributed to a reduction in the average stabilization energy and a decrease in the electronegativity of the system, as listed in [Table II](#).<sup>59</sup>

## E. Radiation shielding and attenuation properties

The radiation shielding and attenuation properties of the new glasses were determined in a wide photon energy range ( $10^{-3}$ – $10^5$  MeV) by using the computer-based program XCOM. The obtained results were also compared with commercial glass shielding<sup>58</sup> and barite concrete.<sup>50</sup> [Fig. 13\(a\)](#) illustrates the relation between the mass attenuation coefficient and the photon energy.

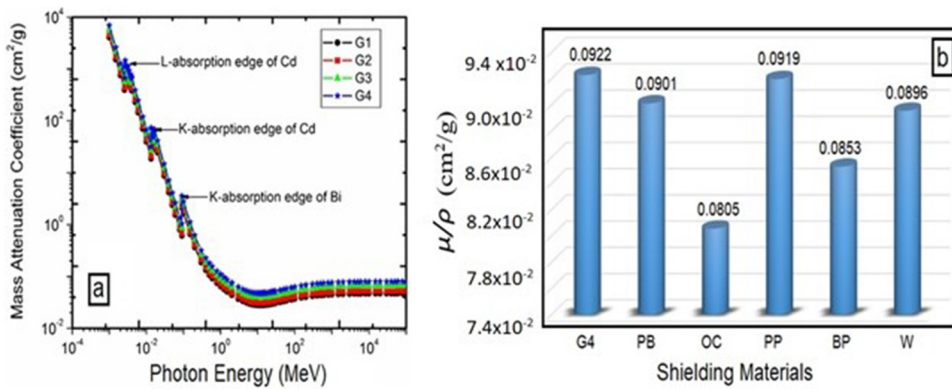


**FIG. 13.** Variation of the mass attenuation coefficient with the photon energy: (a) for the new prepared glasses (G1–G4) and (b) comparison with some shielding materials at 0.6 MeV.

An increase in the photon energies caused a drastic reduction in the mass attenuation coefficient. A constant attenuation coefficient was observed with the continuous increase of photon energy (high megavoltage range  $>10$  MeV). This behavior was attributed to the different possibilities of interaction between photon energy and absorber material at different energies. The attenuation coefficient of the new glass is in direct relation with the CdO content and is very strong at a low energy ( $\sim 4.2 \times 10^3 \text{ cm}^{-1} \text{ g}^{-1}$ ) due to the high photoelectric absorption possibility at this energy level. The possibility of photoelectric absorption is approximately proportional to  $(Z/E)^3$ , where Z is the atomic number of the absorber and E is the photon energy. This possibility increases when the energy of the incident photon is equal or just higher than the electron binding energy.<sup>60</sup>

The attenuation decreases drastically as the photon energy increases. The sharp peaks observed at (0.004 and 0.02 MeV) are due to the L- and K-absorption edges of Cd, and at 0.09 MeV, they are due to the K-absorption edge of bismuth.<sup>58</sup> By increasing the possibility of Compton scattering ( $>150$  keV), the reduction becomes slow. At intermediate energy, the probability of photoelectric absorption is reduced and that of Compton scattering is increased.<sup>60</sup> The interaction probability at this energy is independent of the atomic number of the material and strongly depends on the electron density.<sup>59</sup> At a high energy level, the pair production is dominant and the attenuation coefficient increases slightly and then attains a constant response (10<sup>2</sup> MeV). The achieved results showed that the increment of cadmium oxide to the Bi-B glasses (G<sub>2</sub>-G<sub>4</sub>) resulted in a strong mass attenuation coefficient which was higher than commercial barite concrete and RS 360.

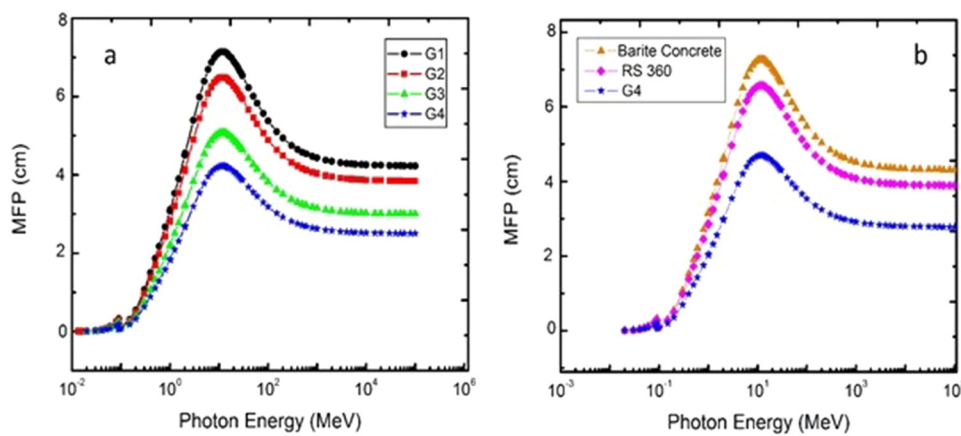
A previous study discussed the effects of CdO and Bi<sub>2</sub>O<sub>3</sub> on glass attenuation and showed the effects of the oxides separately on the shielding properties of glasses.<sup>61</sup> In this study, we investigated the effect of gathering these oxides (CdO and Bi<sub>2</sub>O<sub>3</sub>) in the same glass (borate glass). An enhancement in the mass attenuation coefficients was observed with the increment of CdO, and consequently, an improvement in the other shielding properties of the prepared glasses (HVL, TVL,  $Z_{eff}$ , MFP,...) was expected. Figure 13(b) shows a comparison between the highest mass attenuation coefficients achieved in this study (G4) and some standard

shielding materials such as polyboron, ordinary concrete, pure polyethylene, borated polyethylene, and water at 0.6 MeV.<sup>62</sup>

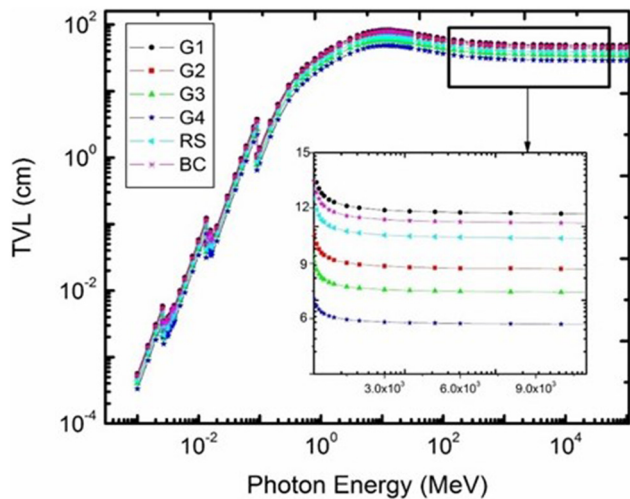
In the current study, we report the variation of shielding properties with the physical and structural properties of the prepared glasses. First, the gradual increase of glass density with the reduction of the bandgap improves the shielding properties. In addition, the compactness of the prepared glasses (reduction of molar volume and increase of molar refraction, OPD, and polarizability) enhances the shielding properties of the new glasses.

Figure 14(a) illustrates the relation between the photon energy and the calculated MFP of the new prepared glasses. For low energies, the MFP increases with an increase of the incident photon energy up to  $\sim 12$  MeV (maximum value), starts decreasing up to  $8 \times 10^2$  MeV, and finally becomes constant up to 10<sup>5</sup> MeV. This behavior may be attributed to the different possibilities of photon interaction with the incident material. The new glasses, especially including CdO content, exhibited a very promising MFP (small values) and their effectiveness improved with increasing CdO concentration. The lowest MFP achieved by G4 (the highest CdO concentration) was also compared with barite concrete and RS 360, as shown in Fig. 14(b). It is clear that the MFP value of G4 is the least compared to the available commercial shielding. The best shielding material is the one that has a smaller MFP (low thickness) with a high incident energy (1/e). Thus, the number of radiation interactions of the photon beam with the target material increases and spontaneously more attenuation is expected.

The tenth value layer (TVL) of the prepared glasses was also determined, as shown in Fig. 15. A close behavior was reported with all prepared glasses. The TVL increased with a high transfer rating at a low energy level and continued to increase (with a slow rating) up to  $\sim 10$  MeV, then decreased and became constant at a high energy ( $>10$  MeV). This behavior was attributed to the variation of interactions of photons at different energies (photoelectric, Compton scattering, and pair production). A promising TVL was achieved by the new glasses (G1-G4) compared with that obtained by barite concrete and RS 360 glass. Concerning the prepared glasses, G4 has the least TVL and hence has the best glass thickness. The glass that can attenuate radiation with a low thickness is cost-effective and is highly recommended for radiation shielding purposes.



**FIG. 14.** (a) Variation of the mean free path with the photon energy for our prepared G1-G4 glass samples and (b) comparison of the new prepared sample G4 with barite concrete<sup>63</sup> and RS 360.<sup>64</sup>



**FIG. 15.** Variation of the tenth value layer (TVL) with the photon energy for new glass samples G1–G4.

Figure 16 shows the effective atomic number ( $Z_{\text{eff}}$ ) of the new glasses in the energy range of 0.01 MeV to 100 MeV. For all samples, a high  $Z_{\text{eff}}$  was observed at the low energy region and it decreased with an increasing photon energy.  $Z_{\text{eff}}$  increased with an increasing CdO content, and this shows that G4 can absorb high-energy photons. A higher  $Z_{\text{eff}}$  was observed at low energy (0.02 MeV) where the photoelectric effect is predominant. A discontinuity in the reduction was observed at the energy level of 0.08 MeV, which was attributed to the K-edge of Bi.<sup>65</sup> The incident photon energy related to K- and L-absorption edges seems to be K (90.53 keV) and 16.39, 15.71,

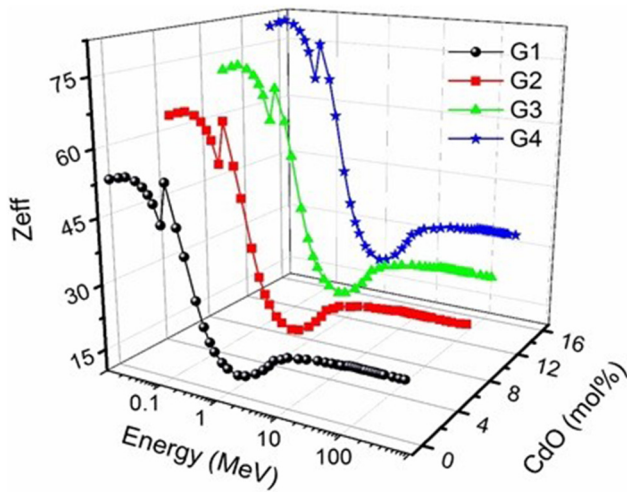


**FIG. 16.** Effective atomic numbers of the prepared glasses at different energy levels (0.01 MeV–10 MeV).

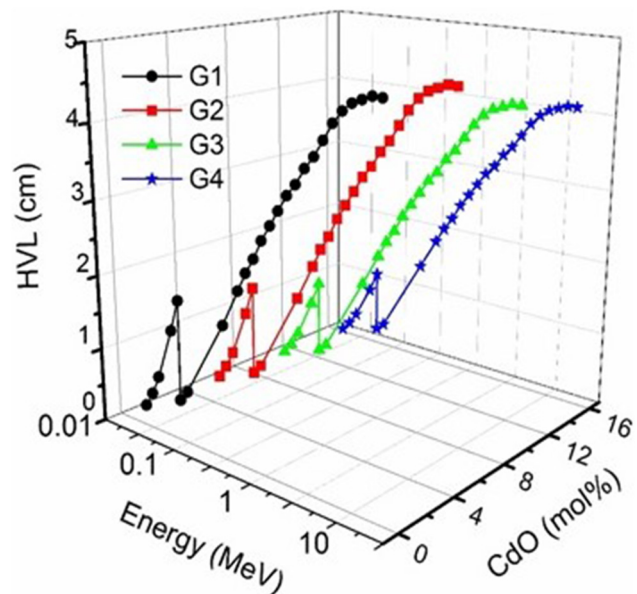


**FIG. 17.** HVL for G1–G4 glasses in the energy range 0.01 MeV to 10 MeV.

and 13.42 keV for  $L_1$ ,  $L_2$ , and  $L_3$ , respectively. Regarding the K absorption edges of the Cd element, the photon absorption occurred at the level of 26.71 keV. The dominant interaction at this energy level is the photo electric absorption.<sup>50</sup> Finally, the  $Z_{\text{eff}}$  values of all prepared glasses (G1–G4) become almost constant at a high energy (independent of photon energy). It is worth mentioning here that the high value of  $Z_{\text{eff}}$  nominates the prepared material to be a competent shielding material.<sup>64–66</sup>

The half-value layer (HVL) values of the prepared glasses were demonstrated over different energy ranges (0.015 MeV–10 MeV), as shown in Fig. 17. In the lower energy level (up to 20 keV), the reported HVLs are nearly constant and quite small. The HVL values range from  $6.18 \times 10^{-5}$  cm for G1 up to  $4.25 \times 10^{-5}$  cm for G4 (decreases by an increasing CdO concentration). It is clear that the HVL starts to increase with increasing photon energy (the highest HVL was recorded at  $\sim 0.05$  MeV). At the energy level  $\sim 100$  keV, the HVLs decrease because of photoelectric absorption dominance.<sup>18, 65</sup> As discussed before, the variation in the HVL values with an increasing energy of the incident photon is attributed to the variation of photon interaction with the glass network. Finally, the HVLs become roughly constant ( $\geq 5$  MeV).

Table V shows the values of the effective electron number (electron density,  $N_e$ ) calculated by using the equation listed in the supplementary material (B). It is reported that  $N_e$  increases by an increasing in the CdO content. This increase may be attributed to the replacement of the lower atomic number element in the current composition (boron-5) by a high atomic number element (cadmium-48). Furthermore, we reported a variation in the  $N_e$  values with an increasing photon energy, and this could be attributed to the changes in the effective atomic number (cross-section dependence) as discussed before.

**TABLE V.** The effective electron number for the newly prepared glasses ( $\times 10^{23}$  electrons/g).

Energy (MeV)	G1	G2	G3	G4
0.010	9.493	9.722	10.185	11.777
0.015	10.694	10.884	11.224	11.848
0.02	10.624	10.945	11.657	12.155
0.03	10.078	10.577	10.824	11.633
0.04	10.011	10.355	10.688	11.465
0.05	9.866	10.033	10.324	11.044
0.06	9.633	9.823	9.994	10.524
0.08	9.882	9.988	10.111	10.884
0.1	9.442	9.544	9.771	10.032
0.2	9.125	9.332	9.443	9.887
0.5	4.011	4.116	4.785	4.892
0.6	3.622	3.703	3.653	3.681
0.8	3.241	3.263	3.284	3.293
1	3.053	3.084	3.075	3.084
2	2.995	3.011	3.022	3.043
3	2.808	2.911	2.995	3.011
4	3.397	3.436	3.417	3.437
5	3.648	3.687	3.668	3.697
6	3.869	3.927	3.894	3.928
8	4.261	4.337	4.314	4.359
9	4.431	4.516	4.483	4.538
10	4.592	4.675	4.654	4.702

#### IV. CONCLUSION

Bismuth borate glasses with different concentrations of cadmium oxide were successfully prepared with the quenching method. The effect of CdO was reported on the structural, physical, and radiation shielding properties. *Ab initio* molecular dynamics simulations were conducted to explain the vibrational density of states of the current composition. The vibration mode of each element in the current composition was determined and compared with the experimental measurements (FTIR and Raman). Furthermore, different radiation properties were estimated at different photon energies (0.01 MeV to 15 MeV). A direct relationship was reported between the CdO and both the mass attenuation coefficient and effective atomic number. The variations in the shielding parameters with fluctuations in the incident photon energy are mostly due to the different cross-section interactions that occur inside the glass network. The calculated MFP, TVL, and HVL showed promising results compared with some standard shielding materials (Concrete and RS 630). The prepared glasses are speculated to be good shielding materials for gamma rays at different medical and industrial facilities. These results will encourage researchers to investigate the shielding properties of particulate radiation (alpha, proton, and neutron) for this new glass composition.

#### SUPPLEMENTARY MATERIAL

The current study includes four [supplementary material](#) sections (A, B, C, and D). (A) includes the mathematical

expressions used for evaluating the physical, optical, and attenuation properties of the prepared glass samples; (B) includes the mathematical expressions for evaluating radiation shielding properties; (C) shows how we calculated the energy bandgap of the prepared glasses; and (D) includes animation movies regarding the elemental vibration of the prepared glasses.

#### ACKNOWLEDGMENTS

The authors would like to gratefully acknowledge the Institute of International Education (IIE)/Fulbright program and NQPI for their financial support and also for the use of the services and facilities of Ohio University. D.A.D. and G.C. thank the National Science Foundation (NSF) under Grant No. DMR-1507670.

#### REFERENCES

- American National Standards Institute (ANSI), *Radiation Safety for X-Ray, Diffraction and Fluorescence Analysis Equipment* (ANSI, New York, 1977), Vol. 43.2.
- M. J. Gardner, A. Hall, M. P. Snee, S. Downes, C. A. Powell, and J. D. Terrell, "Results of case-control study of leukaemia and lymphoma among young people near Sellafield nuclear plant in West Cumbria," *Br. Med. J.* **300**, 423–429 (1990).
- R. R. Wang, A. H. Kumar, P. Tanaka, and A. Macario, "Occupational radiation exposure of anaesthesia providers: A summary of key learning points and resident-led radiation safety projects," *Semin. Cardiothorac. Vasc. Anesth.* **21**, 165–171 (2017).
- C.-M. Lee, Y. H. Lee, and K. J. Lee, "Cracking effect on gamma-ray shielding performance in concrete structure," *Prog. Nucl. Energy* **49**(4), 303–312 (2007).
- N. Singh *et al.*, "Comparative study of lead borate and bismuth lead borate glass systems as gamma-radiation shielding materials," *Nucl. Instrum. Methods Phys. Res. Sect. B* **225** (3), 305–309 (2004).
- T. Kaur, J. Sharma, and T. Singh, "Feasibility of Pb-Zn binary alloys as gamma rays shielding materials," *Int. J. Pure Appl. Phys.* **13**(1), 222–225 (2017).
- S. S. Amritphale, A. Anshul, N. Chandra, and N. Ramakrishnan, "A novel process for making radiopaque materials using bauxite-red mud," *J. Eur. Ceram. Soc.* **27**, 1945–1951 (2007).
- I. F. Al-Hamarneh, "Investigation of gamma-ray shielding effectiveness of natural marble used for external wall cladding of buildings in Riyadh, Saudi Arabia," *Results Phys.* **7**, 1792–1798 (2017).
- I. Akkurt, A. Calik, and H. Akyildirim, "The boronizing effect on the radiation shielding and magnetization properties of AISI 316L austenitic stainless steel," *Nucl. Eng. Des.* **241**(1), 55–58 (2011).
- M. Ambika, N. Nagaiah, and S. Suman, "Role of bismuth oxide as a reinforcer on gamma shielding ability of unsaturated polyester based polymer composites," *J. Appl. Polym. Sci.* **134**(13), 44657 (2017).
- M. Dong *et al.*, "A novel comprehensive utilization of vanadium slag: As gamma ray shielding material," *J. Hazard. Mater.* **318**, 751–757 (2016).
- S. Gupta and G. S. Sidhu, "Gamma-rays absorption studies of garnet series of gemstones at 1 keV to 100 GeV: Theoretical calculation," *IOSR J. Eng.* **4**, 01–08 (2014).
- K. Kirdsiri *et al.*, "Gamma-rays shielding properties of  $x\text{PbO}:(100-x)\text{B}_2\text{O}_3$  glasses system at 662 keV," *Ann. Nucl. Energy* **36**(9), 1360–1365 (2009).
- P. Limkitjaroenporn *et al.*, "Physical, optical, structural and gamma-ray shielding properties of lead sodium borate glasses," *J. Phys. Chem. Solids* **72**(4), 245–251 (2011).
- K. A. Matori *et al.*, "Comprehensive study on physical, elastic and shielding properties of lead zinc phosphate glasses," *J. Non-Cryst. Solids* **457**, 97–103 (2017).
- A. Wagh, Y. Raviprakash, and S. D. Kamath, "Gamma rays interactions with  $\text{Eu}_2\text{O}_3$  doped lead fluoroborate glasses," *J. Alloys Compd.* **695**, 2781–2798 (2017).

- <sup>17</sup>N. Singh, R. Singh, K. J. Singh, and K. Sing, “ $\gamma$ -Ray shielding properties of lead and bismuth borosilicate glasses,” *Glass Technol.* **46**(4), 311–314 (2005).
- <sup>18</sup>P. Glumglomchit *et al.*, “A novel radiation shielding material for gamma-ray: The development of lutetium lithium borate glasses,” *Key Eng. Mater.* **766**, 246–251 (2018).
- <sup>19</sup>P. Kaur, K. J. Singh, and S. Thakur, “Evaluation of the gamma radiation shielding parameters of bismuth modified quaternary glass system,” *AIP Conf. Proc.* **1953**(1), 090031 (2018).
- <sup>20</sup>A. K. Singh, D. Singh, K. S. Thind, and G. S. Mudahar, “Barium-borate-flyash glasses: As radiation shielding materials,” *Nucl. Instrum. Methods Phys. Res. Sect. B* **266**(1), 140 (2008).
- <sup>21</sup>M. H. A. Mhareb, M. A. Almessiere, M. I. Sayyed, and Y. S. M. Alajerami, “Physical, structural, optical and photons attenuation attributes of lithium-magnesium-borate glasses: Role of  $Tm_2O_3$  doping,” *Optik* **182**, 821 (2019).
- <sup>22</sup>G. Lakshminarayana, A. Kumar, M. G. Dong, M. I. Sayyed, N. V. Long, and M. A. Mahdi, “Exploration of gamma radiation shielding features for titanate bismuth borotellurite glasses using relevant software program and Monte Carlo simulation code,” *J. Non-Cryst. Solids* **481**, 65 (2018).
- <sup>23</sup>J. Wang, H. Song, X. Kong, H. Peng, B. Sun, B. Chen, J. Zhang, W. Xu, and H. Xia, “Fluorescence properties of trivalent europium doped in various niobate codoped glasses,” *J. Appl. Phys.* **93**, 1482 (2003).
- <sup>24</sup>Y. S. M. Alajerami, S. Hashim, W. M. S. Wan Hassan, A. T. Ramli, “The effect of CuO and MgO impurities on the optical properties of lithium potassium borate glass,” *Physica B* **407**(13), 2390 (2012).
- <sup>25</sup>M. H. A. Mhareb, S. Hashim, S. K. Ghoshal, Y. S. M. Alajerami, M. A. Saleh, M. M. A. Maqableh, and N. Tamchek, “Optical and erbium ion concentration correlation in lithium magnesium borate glass,” *Optik* **126**(23), 3638 (2015).
- <sup>26</sup>V. Sharma, S. Singh, G. Mudahar, and K. Thind, “Synthesis and characterization of cadmium containing sodium borate glasses,” *New J. Glass Ceram.* **2**(4), 128 (2012).
- <sup>27</sup>S. Bahammam, S. Abd El Al, and F. M. Ezz-Eldin, “Synthesis and characterization of c-irradiated cadmium-borate glasses doped  $V_2O_5$ ,” *Res. Phys.* **7**, 241 (2017).
- <sup>28</sup>E. Pavai and S. P. Dharsini, “Structural and thermal properties of  $B_2O_3$ -CdO-K<sub>2</sub>O glasses,” *Int. J. Recent Sci. Res.* **8**(5), 17242 (2017).
- <sup>29</sup>Y. S. Alajerami, D. Drabold, M. Mhareb, K. L. A. Cimatu, G. Chen, M. Kurudirek, “Radiation shielding properties of bismuth borate glasses doped with different concentrations of cadmium oxides,” *Ceramics International* **46**(8), 12718–12726 (2020).
- <sup>30</sup>P. Pascuta *et al.*, “The local structure of bismuth germanate glasses and glass ceramics doped with europium ions evidenced by FT-IR spectroscopy,” *Vib. Spectrosc.* **48**(2), 281–284 (2008).
- <sup>31</sup>B. Zhou *et al.*, “Superbroadband near-infrared emission in Tm-Bi codoped sodium-germanium-gallate glasses,” *Opt. Express* **19** (7), 6514–6523 (2011).
- <sup>32</sup>P. E. Blöchl, “Projector augmented-wave method,” *Phys. Rev. B* **50**, 17953 (1994).
- <sup>33</sup>G. Kresse and D. Joubert, “From ultrasoft pseudopotentials to the projector augmented-wave method,” *Phys. Rev. B* **59**, 1758 (1999).
- <sup>34</sup>G. Kresse and J. Hafner, “*Ab initio* molecular dynamics for liquid metals,” *Phys. Rev. B* **47**, 558 (1993).
- <sup>35</sup>J. P. Perdew, K. Burke, and M. Ernzerhof, “Generalized gradient approximation made simple,” *Phys. Rev. Lett.* **77**, 3865 (1996).
- <sup>36</sup>D. A. Drabold, “Topics in the theory of amorphous materials,” *Eur. Phys. J. B* **68**, 1 (2009).
- <sup>37</sup>D. J. Evans and B. L. Holian, “The Nose–Hoover thermostat,” *J. Chem. Phys.* **83**, 4069 (1985).
- <sup>38</sup>A. Pasquarello, J. Sarnthein, and R. Car, “Dynamic structure factor of vitreous silica from first principles: Comparison to neutron-inelastic-scattering experiments,” *Phys. Rev. B* **57** 14133 (1998).
- <sup>39</sup>L. Kouvelka *et al.*, “Structure and properties of barium niobophosphate glasses,” *J. Non-Cryst. Solids* **459**, 68 (2017).
- <sup>40</sup>M. J. Berger and J. H. Hubbell, “XCOM: Photon cross sections on a personal computer,” NBSIR 87-3597, National Bureau of Standards (former name of NIST), Gaithersburg, MD 1987.
- <sup>41</sup>V. Dimitrov and S. Sakka, “Electronic oxide polarizability and optical basicity of simple oxides,” *Int. J. Appl. Phys.* **79**(3), 1736 (1996).
- <sup>42</sup>M. N. Azlan, M. K. Halimah, S. Z. Shafinas, and W. M. Daud, “Polarizability and optical basicity of  $Er^{3+}$  ions doped tellurite based glasses,” *Chalcogenide Lett.* **11**(7), 319 (2014).
- <sup>43</sup>M. Z. Azlan, M. K. Halimah, S. Z. Shafinas, and W. M. Daud, “Electronic polarizability of zinc borotellurite glass system containing erbium nanoparticles,” *Mater. Express.* **5**(3), 211 (2015).
- <sup>44</sup>B. Bhatia, S. L. Meena, V. Parihar, and M. Poonia, “Optical basicity and polarizability of  $Nd^{3+}$  doped bismuth borate glasses,” *New J. Glass Ceram.* **5**, 44 (2015).
- <sup>45</sup>P. Kaur, K. J. Singh, M. Kurudirek, and S. Thakur, “Study of environment friendly bismuth incorporated lithium borate glass system for structural, gamma-ray and fast neutron shielding properties,” *Spectrochim. Acta Part A* **223**, 117309 (2019).
- <sup>46</sup>D. Turnbull, “Under what conditions can a glass be formed?,” *Contemp. Phys.* **10**, 473 (1969).
- <sup>47</sup>H. E. Atiya and A. S. Farid, “Non-isothermal crystallization kinetics of ternary  $Se_{90}Te_{10-x}Pb_x$  glasses,” *J. Cryst. Growth* **436**, 125 (2016).
- <sup>48</sup>S. Rejisha *et al.*, “Synthesis and characterization of strontium and barium bismuth borate glass-ceramics,” *J. Non-Cryst. Solids* **388**, 68 (2014).
- <sup>49</sup>S. Rani *et al.*, “Influence of  $Bi_2O_3$  on thermal, structural and dielectric properties of lithium zinc bismuth borate glasses,” *J. Alloys Cmpd.* **597**, 110 (2014).
- <sup>50</sup>P. Kaur, K. J. Singh, S. Thakur, P. Singh, and B. S. Bajwa, “Investigation of bismuth borate glass system modified with barium for structural and gamma-ray shielding properties,” *Spectrochim. Acta Part A* **206**, 367 (2019).
- <sup>51</sup>K. Kaur, K. Singh, and V. Anand, “Structural properties of  $Bi_2O_3$ - $B_2O_3$ - $SiO_2$ - $Na_2O$  glasses for gamma ray shielding applications,” *Radiat. Phys. Chem.* **120**, 63 (2016).
- <sup>52</sup>J. E. Shelby and J. Ruller, “Properties of barium gallium germanate glasses,” *Phys. Chem. Glasses* **28**, 262 (1987).
- <sup>53</sup>X. Y. Zhao, X. L. Wang, H. Lin, and Z. Q. Wang, “Electronic polarizability and optical basicity of lanthanide oxides,” *Physica B* **392**, 132 (2007).
- <sup>54</sup>M. M. Ahmed, C. A. Hogarth, and M. N. Khan, “A study of the electrical and optical properties of the  $GeO_2$ - $TeO_2$  glass system,” *J. Mater. Sci.* **19**, 4040 (1984).
- <sup>55</sup>M. E. Lines *et al.*, “Absolute Raman intensities in glasses,” *J. Non-Cryst. Solids* **89**(1), 163 (1987).
- <sup>56</sup>G. D. Chrysikkos and E. I. Kamitsos, “A Raman investigation of cadmium borate and borogermanate glasses,” *J. Non-Cryst. Solids* **93**, 155 (1987).
- <sup>57</sup>A. Kumar, R. Kaur, M. I. Sayyed, M. Rshad, M. Singh, and A. M. Ali, “Physical, structural, optical and gamma ray shielding behavior of  $(20+x)$   $PbO$ - $10$   $BaO$ - $10$   $Na_2O$ - $10$   $MgO$ - $(50-x)$   $B_2O_3$  glasses,” *Phys. B Condens. Matter.* **552**, 110 (2019).
- <sup>58</sup>D. Sing, S. Kumar, and R. Thangaraj, “Study of the physical properties with compositional dependence in  $(S_270Ge_30)100-xBix$  ( $0 < x < 8$ ) glassy semiconductors,” *Adv. Appl. Sci. Res.* **2**(3), 20 (2011).
- <sup>59</sup>J. F. Eloy, *Power Lasers, National School of Physics* (John Wiley and Sons, Grenoble, France, 2011), p. 59.
- <sup>60</sup>A.-H. Benali and G. M. Ishak-Boushaki, “Energy response of FD-7 RPL glass dosimeter compared with LiF Mg, Ti and  $Al_2O_3:C$  dosimeters,” *J. Instrum.* **13**, P11015 (2018).
- <sup>61</sup>Y. B. Saddeek, S. A. M. Issa, T. Alharbi, K. Aly, M. Ahmad, and H. O. Tekin, “Mechanical and nuclear shielding properties of sodium cadmium borate glasses: Impact of cadmium oxide additive,” *Ceram. Int.* **46**(3), 2661–2669 (2020).
- <sup>62</sup>R. Biswas, H. Sahadath, A. S. Mollah, and M. F. Huq, “Calculation of gamma-ray attenuation parameters for locally developed shielding material: Polyboron,” *J. Radiat. Res. Appl. Sci.* **9**, 26–34 (2016).

<sup>63</sup>K. Singh, N. Singh, R. S. Kaundal, and K. Singh, "Gamma-ray shielding and structural properties of PbO-SiO<sub>2</sub> glasses," *Nucl. Instrum. Methods Phys. Res. Sect. B*, **266**(6), 944 (2008).

<sup>64</sup>M. Almatari, O. Agar, E. E. Altunsoy, O. Kilicoglu, M. I. Sayyed, and H. O. Tekin, "Photon and neutron shielding characteristics of samarium doped lead alumino borate glasses containing barium, lithium and zinc oxides determined at medical diagnostic energies," *Res. Phys.*, **12**, 2123 (2019).

<sup>65</sup>M. G. Dong, M. I. Sayyed, M. Çelikbilek Ersundu, A. E. ErsundudPriyank Nayar, and M. A. Mahdi, "Investigation of gamma radiation shielding properties of lithium zinc bismuth borate glasses using XCOM program and MCNP5 code," *J. Non-Crystal. Solids*, **468**, 12 (2017).

<sup>66</sup>R. S. Kaundal, "Comparative study of radiation shielding parameters for bismuth borate glasses," *Mater. Res.*, **19**(4), 776 (2016).